

## A Preliminary Calculation of Three-Dimensional Unsteady Underwater Cavitating Flows Near Incompressible Limit

Yang-Yao Niu\* and Wei-Yuan Hsu

*Department of Mechanical Engineering, Chung-Hua University, Hsin-Chu, Taiwan, 30067, ROC.*

Received 9 October 2007; Accepted (in revised version) 10 December 2007

Communicated by Kun Xu

Available online 29 May 2008

---

**Abstract.** Recently, cavitated flows over underwater submerged bodies have attracted researchers to simulate large scale cavitation. Comparatively Computational Fluid Dynamics (CFD) approaches have been used widely and successfully to model developed cavitation. However, it is still a great challenge to accurately predict cavitated flow phenomena associated with interface capturing, viscous effects, unsteadiness and three-dimensionality. In this study, we consider the preconditioned three-dimensional multiphase Navier-Stokes equations comprised of the mixture density, mixture momentum and constituent volume fraction equations. A dual-time implicit formulation with LU Decomposition is employed to accommodate the inherently unsteady physics. Also, we adopt the Roe flux splitting method to deal with flux discretization in space. Moreover, time-derivative preconditioning is used to ensure well-conditioned eigenvalues of the high density ratio two-phase flow system to achieve computational efficiency. Validation cases include an unsteady 3-D cylindrical headform cavitated flow and an 2-D convergent-divergent nozzle channel cavity-problem.

**AMS subject classifications:** 76B10, 76D05, 65M10

**Key words:** Cavitation, incompressible, Roe Riemann solver, dual-time stepping.

---

### 1 Introduction

Cavitation is one of important phenomena in the hydrodynamics problems. Cavitation is well known to associate with three aspects: formation, growth and collapse of bubbles within the body of a liquid due to the process of nucleation in a liquid flow where

---

\*Corresponding author. *Email addresses:* yniu@chu.edu.tw (Y.-Y. Niu), m09408021@chu.edu.tw (W.-Y. Hsu)

the pressure falls below the vapor pressure. This phenomenon usually arises in flows around solid bodies, the turning corner of convergent nozzle, leading edge of the blades and tip leakage. It strongly affects the flow field to induce severe noise and structural erosion which result in supplementary maintenance operations of the turbomachinery and pump.

One pattern of cavitating flows might occur partially on the body surface or it might grow until it becomes very long compared with the body dimensions. It is always denoted as the super-cavitation which has been successfully formulated as near steady-state and incompressible flow models [1]. However, in high speed supercavitating flows around underwater projectiles, dramatic increase of void propagation associated with unsteady mass transferring dynamics gives rise to the cloud collapse physics. The large transient variation of interfacial dynamics such as density, void fraction and viscosity gradients around the interfaces naturally attract unsteady formulation of numerical method constructed. Several numerical methods had been proposed in the past in order to simulate the related phenomena in cavitation flows, such as the VOF method [2,3], the level set method [4] and the interface capturing method [5]. Recently, one common approach to combine the VOF model with the interface capturing scheme to constitute the so-called Eulerian approach based on separated equations to describe different fluids or phases. Several different Eulerian formulations are usually used to capture the interface, namely the multi-fluid model [6–9], the mixture model [10–17] and the ghost cell model [18].

The multi-fluid model containing individual particles, droplets or bubbles is through the so-called two-fluid model, in which the time or space ensemble average process is applied to both the continuous and disperse phase. Two sets of Navier-Stokes equations are used to describe both phases of fluids with additional inter-phasic terms for the exchange of momentum and energy between phases. Since each phase has its own velocity and temperature, the two-fluid model allows both mechanical and thermal non-equilibrium to be considered in the modeling; in that respect, it represents a more general model for two-phase flows. Two-fluid model have also been utilized for natural cavitation. However, in super-cavity flows, the gas-liquid interface is known to be nearly in dynamic equilibrium; for this reason, we do not pursue a full two-fluid level of modeling. In the mixture model, the mass, momentum and energy of the multi-phase flow are described by a set of Navier-Stokes equations. Usually among the mixture model, a single continuity equation is considered with the abrupt variations of density between vapor and liquid phases through a condensation-evaporation process. Such single-continuity-equation-homogeneous type mixture methods have become fairly widely used for sheet and supercavitating flow analysis [1, 10–16]. Here, a time-accurate preconditioned type three-dimensional multiphase Navier-Stokes analysis near the limit of incompressible flow is extended based on the mixture flow model for the prediction of underwater cavitation problems. A dual-time stepping method is used for the unsteady computations by introducing artificial time terms in the governing equations and highly accurate resolution of phase interfaces will be introduced.

The paper is organized as follows. In Section 2, the governing equations will be pre-

sented. The numerical methods will be described in Section 3. Numerical results on cavitated flows over a 3D cylindrical headform and on a 2D channel cavity will be reported and discussed. Some concluding remarks will be given in the final section.

## 2 Governing equations

In the mixture flow model, the flow is assumed to be in thermal and dynamic equilibrium at the interface where the flow velocity is assumed to be continuous. Therefore, the equations are described as a fluid mixture of liquid and vapor. The phasic continuity equations are written in terms of the volume fraction to simplify the derivation of the eigensystem. Source terms are added to the mixture continuity equation to model the mass-transfer rates  $\dot{S}$  from liquid to vapor and from vapor to liquid. The governing equations can be written in the following generalized curvilinear coordinates as

$$\Gamma_e \frac{\partial \hat{Q}}{\partial t} + \Gamma \frac{\partial \hat{Q}}{\partial \tau} + \frac{\partial(F - F_v)}{\partial \xi} + \frac{\partial(G - G_v)}{\partial \eta} + \frac{\partial(H - H_v)}{\partial \zeta} = S, \tag{2.1}$$

where

$$\hat{Q} = \frac{Q}{J} = \frac{1}{J} \begin{pmatrix} p \\ u \\ v \\ w \\ \alpha_g \end{pmatrix}; \quad F = \frac{1}{J} \begin{pmatrix} U \\ \rho_m u U + \xi_x p \\ \rho_m v U + \xi_y p \\ \rho_m w U + \xi_z p \\ \alpha_g U \end{pmatrix}; \quad G = \frac{1}{J} \begin{pmatrix} V \\ \rho_m u V + \eta_x p \\ \rho_m v V + \eta_y p \\ \rho_m w V + \eta_z p \\ \alpha_g V \end{pmatrix}; \quad H = \frac{1}{J} \begin{pmatrix} W \\ \rho_m u W + \zeta_x p \\ \rho_m v W + \zeta_y p \\ \rho_m w W + \zeta_z p \\ \alpha_g W \end{pmatrix},$$

where the subscripts  $l$  and  $g$  denote the liquid phase and the vapor phase, respectively,  $J$  is the transform Jacobian matrix from the generalized coordinates to the Cartesian coordinates,  $p$  is the pressure,  $(u, v, w)$  are the velocity components in  $x, y, z$  direction, respectively,  $\alpha_g$  is the gas volume fraction. The contravariant velocity  $U$  in the  $\xi$  direction is defined by

$$U = \xi_x u + \xi_y v + \xi_z w + \xi_t. \tag{2.2}$$

Similar forms can be obtained for  $V$  and  $W$ . Also, the viscous fluxes can be given by

$$F_v = \frac{\mu}{JRe} \begin{pmatrix} 0 \\ (\nabla \xi \cdot \nabla \xi) \frac{\partial u}{\partial \xi} + (\nabla \xi \cdot \nabla \eta) \frac{\partial u}{\partial \eta} + (\nabla \xi \cdot \nabla \zeta) \frac{\partial u}{\partial \zeta} \\ (\nabla \xi \cdot \nabla \xi) \frac{\partial v}{\partial \xi} + (\nabla \xi \cdot \nabla \eta) \frac{\partial v}{\partial \eta} + (\nabla \xi \cdot \nabla \zeta) \frac{\partial v}{\partial \zeta} \\ (\nabla \xi \cdot \nabla \xi) \frac{\partial w}{\partial \xi} + (\nabla \xi \cdot \nabla \eta) \frac{\partial w}{\partial \eta} + (\nabla \xi \cdot \nabla \zeta) \frac{\partial w}{\partial \zeta} \\ 0 \end{pmatrix}. \tag{2.3}$$

Similar forms can be obtained for  $G_v$  and  $H_v$ . Moreover,

$$S = \frac{1}{J} \{0, 0, 0, 0, (\dot{S}_v)\}^T. \tag{2.4}$$

In addition, a vapor generation source term originally used by Kunz et al. [10] is used to model the cavitation event. In their model, the mass transfer rate is proportional to the volume fraction and the amount of the local pressure less or more than the vapor pressure:

$$\dot{S} = \alpha_l \left( \frac{c_{\text{prod}}}{t_\infty} \max(0, p_v - p) - \frac{c_{\text{evap}}}{t_\infty} \alpha_l \alpha_g \right), \tag{2.5}$$

where  $t_\infty$  denotes the characteristic time and  $p_v$  is the vapor pressure. The constants  $(c_{\text{evap}}/t_\infty)$  and  $(c_{\text{prod}}/t_\infty)$  are empirical, which express the time rate of the evaporation and condensation processes with respect to the flow process. In this work,  $c_{\text{evap}}/t_\infty = 0.01$  and  $c_{\text{prod}}/t_\infty = 5$  for  $p_g/p_l = 0.001$ . Furthermore, the transformation matrices  $\Gamma_e$  and  $\Gamma$  from conservative variables to primitive variables are given by

$$\Gamma_e = \begin{pmatrix} 0 & 0 & 0 & 0 & 0 \\ 0 & \rho_m & 0 & 0 & u(\rho_g - \rho_l) \\ 0 & 0 & \rho_m & 0 & v(\rho_g - \rho_l) \\ 0 & 0 & 0 & \rho_m & w(\rho_g - \rho_l) \\ 0 & 0 & 0 & 0 & 1 \end{pmatrix}; \quad \Gamma = \begin{pmatrix} 1/\beta & 0 & 0 & 0 & 0 \\ 0 & \rho_m & 0 & 0 & u(\rho_g - \rho_l) \\ 0 & 0 & \rho_m & 0 & v(\rho_g - \rho_l) \\ 0 & 0 & 0 & \rho_m & w(\rho_g - \rho_l) \\ \alpha_g/\beta & 0 & 0 & 0 & 1 \end{pmatrix}. \tag{2.6}$$

At the same time, the mixture density can be calculated based on the volume fraction and the phasic density as follows:

$$\rho_m = \alpha_l \rho_l + \alpha_g \rho_g, \quad \alpha_l + \alpha_g = 1. \tag{2.7}$$

Besides, the governing equations are normalized with the liquid density  $\rho_l$ , free stream velocity  $U_\infty$  and the characteristic length of the body  $D$ . Therefore, the Reynolds number is defined as

$$\text{Re} = \frac{\rho_l U_\infty D}{\mu_l}. \tag{2.8}$$

Based on the artificial compressibility parameter  $\beta$ ,  $\tau$  in (2.1) is the artificial characteristic time, and  $t$  is the physical time. The artificial time terms are added to the governing equations in order to build up a dual-time stepping algorithm for the unsteady calculations. The proposed artificial terms ensure a consistent convergence rate. In this *baseline* formulation, the phasic density of each constituent is taken as constant. Also, note that each of the equations contains two sets of time-derivatives — those written in terms of the variable “ $t$ ” correspond to physical time terms, while those written in terms of “ $\tau$ ” correspond to pseudo-time terms that are employed in the time-iterative solution procedure. The forms of the pseudo-time terms will be discussed in the next section.

### 3 Numerical discretization

Here, the main algorithm for the solution of the time dependent preconditioned Navier-Stokes equations [19,20] is presented. Numerical methods include the dual-time stepping

for a time-derivative preconditioning model, Roe type flux calculations [21] at cell interfaces based on the characteristics of the governing equations and a linearized implicit solution of the resulting non-linear system. Therefore, the eigenvalues and eigenvectors of the incompressible multi-phase system equations are required for the numerical discretization of the convective flux. Eq. (2.1) can be linearized first as

$$\frac{\partial \hat{Q}}{\partial \tau} + \Gamma^{-1} \Gamma_e \frac{\partial \hat{Q}}{\partial t} + \Gamma^{-1} A \frac{\partial \hat{Q}}{\partial \xi} + \Gamma^{-1} B \frac{\partial \hat{Q}}{\partial \eta} + \Gamma^{-1} C \frac{\partial \hat{Q}}{\partial \zeta} = \Gamma^{-1} S = \hat{S}, \tag{3.1}$$

where  $A = \partial F / \partial Q$ , similarly for  $B$  and  $C$ . The matrix  $\tilde{A} = T^{-1} \partial F / \partial Q$  is given by

$$\tilde{A} = \begin{pmatrix} 0 & \zeta_x \beta & \zeta_y \beta & \zeta_z \beta & 0 \\ \frac{\zeta_x}{\rho_m} & \zeta_x u + U & \zeta_y u & \zeta_z u & 0 \\ \frac{\zeta_y}{\rho_m} & \zeta_y v & \zeta_y v + U & \zeta_z v & 0 \\ \frac{\zeta_z}{\rho_m} & \zeta_z w & \zeta_z w & \zeta_z w + U & 0 \\ 0 & 0 & 0 & 0 & U \end{pmatrix}. \tag{3.2}$$

The eigenvalues of the preconditioned Jacobian matrix  $\tilde{A}$  are given by

$$\lambda_1, \lambda_2, \lambda_5 = U, \quad \lambda_3 = U + C, \quad \lambda_4 = U - C, \quad C = \sqrt{U^2 + \beta(\zeta_x^2 + \zeta_y^2 + \zeta_z^2) / \rho_m}. \tag{3.3}$$

The eigenvector matrix is given by

$$X = \begin{pmatrix} 0 & 0 & \beta C & -\beta C & 0 \\ m_x & n_x & u \lambda_3 + \frac{\beta \zeta_x}{\rho_m} & u \lambda_4 + \frac{\beta \zeta_x}{\rho_m} & 0 \\ m_y & n_y & v \lambda_3 + \frac{\beta \zeta_y}{\rho_m} & v \lambda_4 + \frac{\beta \zeta_y}{\rho_m} & 0 \\ m_z & n_z & w \lambda_3 + \frac{\beta \zeta_z}{\rho_m} & w \lambda_4 + \frac{\beta \zeta_z}{\rho_m} & 0 \\ 0 & 0 & 0 & 0 & 1 \end{pmatrix}, \tag{3.4}$$

where  $(m_x, m_y, m_z), (n_x, n_y, n_z)$  can be constructed to be linear independent based on geometry metrics and orthogonal to the local surface vector. The construction procedure can be found in the works of Pan and Chakravarthy [22].

### 3.1 Time discretization

In the dual-time stepping formulation, usually, the physical-time terms are discretized using a second-order, three-point, backward difference formula; that is

$$\Gamma_e \frac{\partial \hat{Q}}{\partial t} = \Gamma_e \frac{1.5 \hat{Q}^{n+1, k+1} - 2 \hat{Q}^n + 0.5 \hat{Q}^{n-1}}{\Delta t}, \tag{3.5}$$

where  $n$  designates the index of the physical-time level and  $k$  is the index of the artificial-time level. The artificial-time terms are discretized by the following implicit Euler finite-difference formula:

$$\Gamma \frac{\partial \hat{Q}}{\partial \tau} = \Gamma \frac{\hat{Q}^{n+1,k+1} - \hat{Q}^{n+1,k}}{\Delta \tau}. \tag{3.6}$$

Based on Eqs. (3.5) and (3.6), the linearized form of Eq. (3.1) can be written as

$$\begin{aligned} & \left( \Gamma_e \frac{1.5}{J\Delta t} + \Gamma \frac{1}{J\Delta \tau} + \frac{\partial A}{\partial \xi} + \frac{\partial B}{\partial \eta} + \frac{\partial C}{\partial \zeta} - \frac{\partial A_v}{\partial \xi} - \frac{\partial B_v}{\partial \eta} - \frac{\partial C_v}{\partial \zeta} - \frac{\partial \hat{S}}{\partial \hat{Q}} \right)^{n+1,k} \Delta \hat{Q}^{n+1,k+1} \\ &= \Gamma_e \frac{1.5\hat{Q}^{n+1,k} - 2\hat{Q}^{n,k} + 0.5\hat{Q}^{n-1,k}}{\Delta t} - \left( \frac{\partial(F-F_v)}{\partial \xi} + \frac{\partial(G-G_v)}{\partial \eta} + \frac{\partial(H-H_v)}{\partial \zeta} + \hat{S} \right)^{n+1,k} \\ &= \text{Res}(\hat{Q}). \end{aligned} \tag{3.7}$$

Then we can simplify Eq. (3.7) by the following delta form

$$\begin{aligned} & \left( 1 + \frac{3\Delta \tau}{2\Delta t} \Gamma^{-1} \Gamma_e + \Gamma^{-1} J \Delta \tau \left( \frac{\partial A}{\partial \xi} + \frac{\partial B}{\partial \eta} + \frac{\partial C}{\partial \zeta} - \frac{\partial A_v}{\partial \xi} - \frac{\partial B_v}{\partial \eta} - \frac{\partial C_v}{\partial \zeta} - \frac{\partial \hat{S}}{\partial \hat{Q}} \right) \right)^{n+1,k} \Delta \hat{Q}^{n+1,k+1} \\ &= \Gamma^{-1} J \Delta \tau \text{Res}(\hat{Q})^{n+1,k}. \end{aligned} \tag{3.8}$$

The above equation can be factorized using the LU decomposition method for the pseudo time iteration;  $\text{Res}(\hat{Q})$  is the unsteady residue vector,  $\Delta \hat{Q}$  is the spatial difference  $\hat{Q}_{i+1} - \hat{Q}_i$ ;  $\Delta \tau$  is chosen as the local pseudo time step which is determined by the largest eigenvalue of the preconditioning system of the governing equations for each grid cell. The diffusion terms are evaluated by the standard central differencing scheme. The implicit part at the left-hand side of Eq. (3.8) is discretized using a first-order upwind difference scheme. One of them in the  $\xi$  direction can be expressed as:

$$\frac{\partial A}{\partial \xi} = \frac{(A_{i+1,j,k} - A_{i,j,k})}{\Delta \xi}, \tag{3.9}$$

where  $A = A^+ + A^-$ , and  $A^+$  and  $A^-$  are computed based on the eigenvalues of the matrix  $A$  and the related eigenvector  $T$ , namely,

$$A^\pm = T \Lambda^\pm T^{-1}, \text{ with} \tag{3.10}$$

$$\Lambda = \begin{pmatrix} \lambda_1 & 0 & 0 & 0 & 0 \\ 0 & \lambda_2 & 0 & 0 & 0 \\ 0 & 0 & \lambda_3 & 0 & 0 \\ 0 & 0 & 0 & \lambda_4 & 0 \\ 0 & 0 & 0 & 0 & \lambda_5 \end{pmatrix}. \tag{3.11}$$

The terms for  $B$  and  $C$  can be treated similarly. Eq. (3.8) can be factorized after using finite difference formulation for the derivative term:

$$[(D-L)D^{-1}(D+U)]\Delta \hat{Q}_{i,j,k}^{n+1,k+1} = \Gamma^{-1} J \Delta \tau \text{Res}(\hat{Q})^{n+1,k}, \tag{3.12}$$

where  $L$ ,  $D$  and  $U$  are recursively as:

$$L = \Gamma^{-1} \frac{\Delta\tau}{\Delta\zeta} \left[ -A_{i-1,j,k}^+ + \frac{1}{2}(A_v)_{i-1,j,k} \right] + \Gamma^{-1} \frac{\Delta\tau}{\Delta\eta} \left[ -B_{i,j-1,k}^+ + \frac{1}{2}(B_v)_{i,j-1,k} \right] + \Gamma^{-1} \frac{\Delta\tau}{\Delta\zeta} \left[ -C_{i,j,k-1}^+ + \frac{1}{2}(C_v)_{i,j,k-1} \right], \tag{3.13}$$

$$D = I + \Gamma_\omega \Gamma^{-1} \frac{3\Delta\tau}{2\Delta t} + \Gamma^{-1} \frac{\Delta\tau}{\Delta\zeta} \left[ A_{i,j,k} - \frac{1}{2}(A_v)_{i,j,k} \right] + \Gamma^{-1} \frac{\Delta\tau}{\Delta\eta} \left[ B_{i,j,k} - \frac{1}{2}(B_v)_{i,j,k} \right] + \Gamma^{-1} \frac{\Delta\tau}{\Delta\zeta} \left[ C_{i,j,k} - \frac{1}{2}(C_v)_{i,j,k} \right], \tag{3.14}$$

$$U = \Gamma^{-1} \frac{\Delta\tau}{\Delta\zeta} \left[ A_{i+1,j,k}^+ - \frac{1}{2}(A_v)_{i+1,j,k} \right] + \Gamma^{-1} \frac{\Delta\tau}{\Delta\eta} \left[ B_{i,j+1,k}^+ - \frac{1}{2}(B_v)_{i,j+1,k} \right] + \Gamma^{-1} \frac{\Delta\tau}{\Delta\zeta} \left[ C_{i,j,k+1}^+ - \frac{1}{2}(C_v)_{i,j,k+1} \right]. \tag{3.15}$$

Furthermore, Eq. (3.12) can be proceeded using the LU approach to advance the solution in pseudo-time. This is implemented in two steps, i.e., a backward and a forward step in each direction:

$$\text{first } (D - L)\Delta\hat{Q}^* = RHS_{i,j,k}^{n+1,k+1/2}, \tag{3.16}$$

$$\text{then } (D + U)\Delta\hat{Q}_{i,j,k}^{n+1,k+1} = D\Delta\hat{Q}^*. \tag{3.17}$$

Finally, the primitive variables at the new pseudo-time level  $k+1$  is updated by

$$\hat{Q}_{i,j,k}^{n+1,k+1} = \hat{Q}_{i,j,k}^{n+1,k} + \Delta\hat{Q}^*. \tag{3.18}$$

### 3.2 Numerical flux

Considering the derivative of the convective flux in the  $\zeta$ -direction, we use the following difference formula for the flux derivatives:

$$\frac{\partial F}{\partial \zeta} = \frac{F_{i+1/2,j,k} - F_{i-1/2,j,k}}{\Delta\zeta}. \tag{3.19}$$

The convective flux at the cell interfaces is computed by the Roe type flux-difference splitting. The flux difference splitting scheme is constructed based on the eigenvalues and eigenvectors of the Jacobian matrix  $\tilde{A}$ . This approach admits that numerical flux  $F$  contains the characteristic information propagating through the domain, with speed and direction according to the eigenvalues of the system. By splitting  $F$  into different parts, where each part contains the information traveling in a particular direction, i.e., characteristic information, and by differencing the split fluxes according to the directions

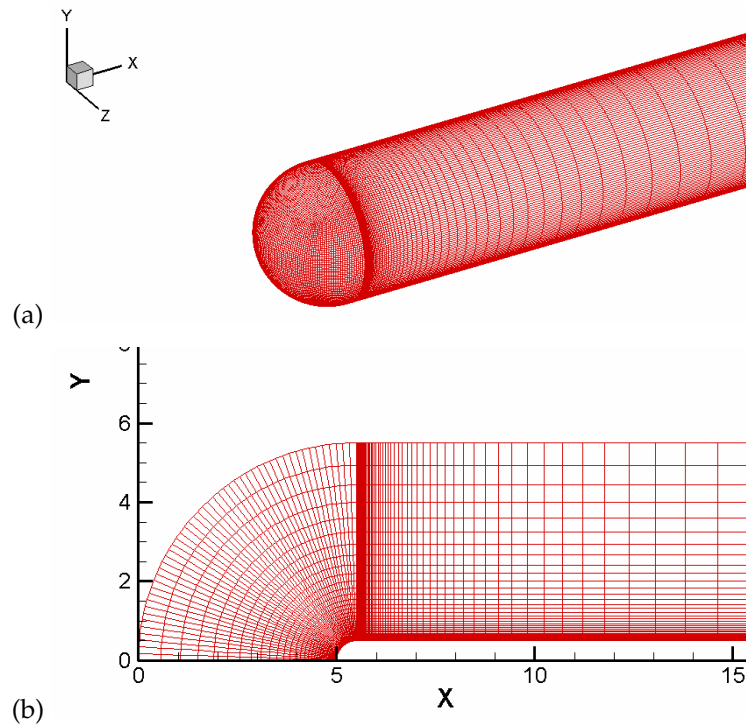


Figure 1: (a) The surface mesh distributions for the cylindrical headform ( $60 \times 50 \times 100$ , C type grid points). (b) 2D side view of mesh distributions for the cylindrical headform.

of the corresponding wave propagation, the interface numerical flux of each cell is then expressed as

$$F_{i+1/2,j,k} = \frac{1}{2} (F_{i+1,j,k} + F_{i,j,k}) - \frac{1}{2} (\Gamma T |\Lambda| T^{-1})_{i+1/2,j,k} \Delta Q_{i+1/2,j,k}. \quad (3.20)$$

Here  $\Delta Q$  is the spatial difference  $Q_{i+1} - Q_i$ .

## 4 Results and discussions

In the verification, cavitated flows over a 3D cylindrical headform and 2D convergent/divergent channel are chosen and compared with experimental data [23,24]. Especially, the two-dimensional simulations of the cylindrical headform can be found in many literatures as [10–14, 16, 17]. In these past works, the numerical results in the cases of large cavitation number have achieved accurate computations against measurement. However, the simulations of low cavitation number as 0.2 or 0.3 are not satisfactory. Also, the three-dimensional computations of cylindrical headform have seldom been seen in the past works.

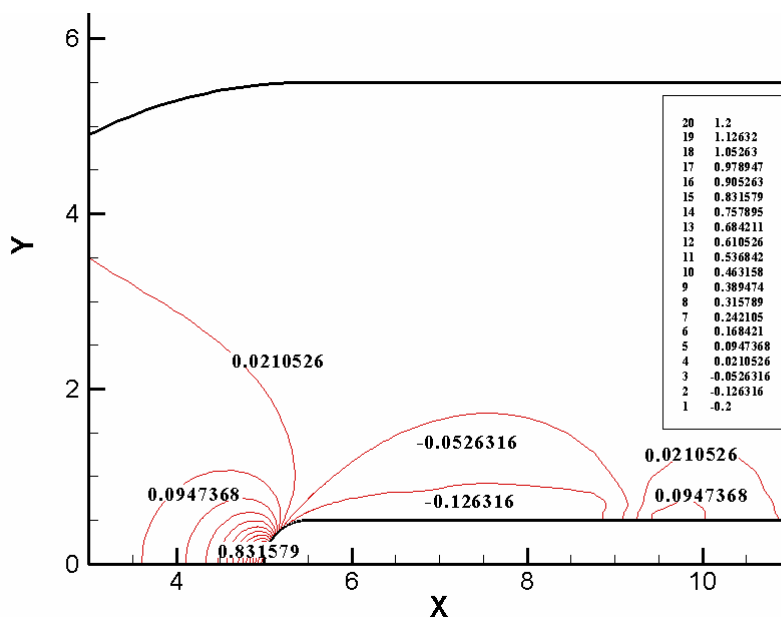


Figure 2: 2D side view of pressure coefficient distribution ( $K=0.2$ ).

#### 4.1 Cylindrical headform

A measurement data achieved on a wind tunnel conducted by Rouse and McNown [23], involving liquid water flow over a cylindrical forebody, is chosen as the first verification test case in this work. The experiment of Rouse and McNown has been widely used for the assessment of incompressible flow models for cavitation prediction. Flow conditions are assumed for each computation with the same Reynolds number of  $1.36 \times 10^5$ , temperature of 300K, incoming uniform velocity of 4.317 m/s. Also, the incompressible flow liquid density is  $998.2 \text{ kg/m}^3$  at standard conditions. The surface pressure distributions considered as functions of the cavitation number are used for the comparison against measurement. The grid independence study is performed on the comparison of predicted surface pressure coefficient against the measured data of Rouse and McNown as seen in Fig. 4. The computed results on coarse and fine grids are almost identical. Therefore, we only demonstrate the results on coarse grids in this section. The influence the cavitation number on occurrence of cavitation is studied. Under the above-mentioned conditions, the vapor pressure is set to be 3589Pa. Standard subsonic inflow (fixed velocity and extrapolated pressure) and subsonic out flow (fixed pressure and extrapolated velocity) are used in the calculations. In addition, the computations are performed on the C-type mesh with  $60 \times 50 \times 100$  and  $60 \times 75 \times 200$  nodes. As shown in Figs. 1(a) and 1(b), the  $60 \times 50 \times 100$  grid plot is clustered tightly to the body surface and to the region downstream of the end of the cylindrical section, where a cavity growth is expected.

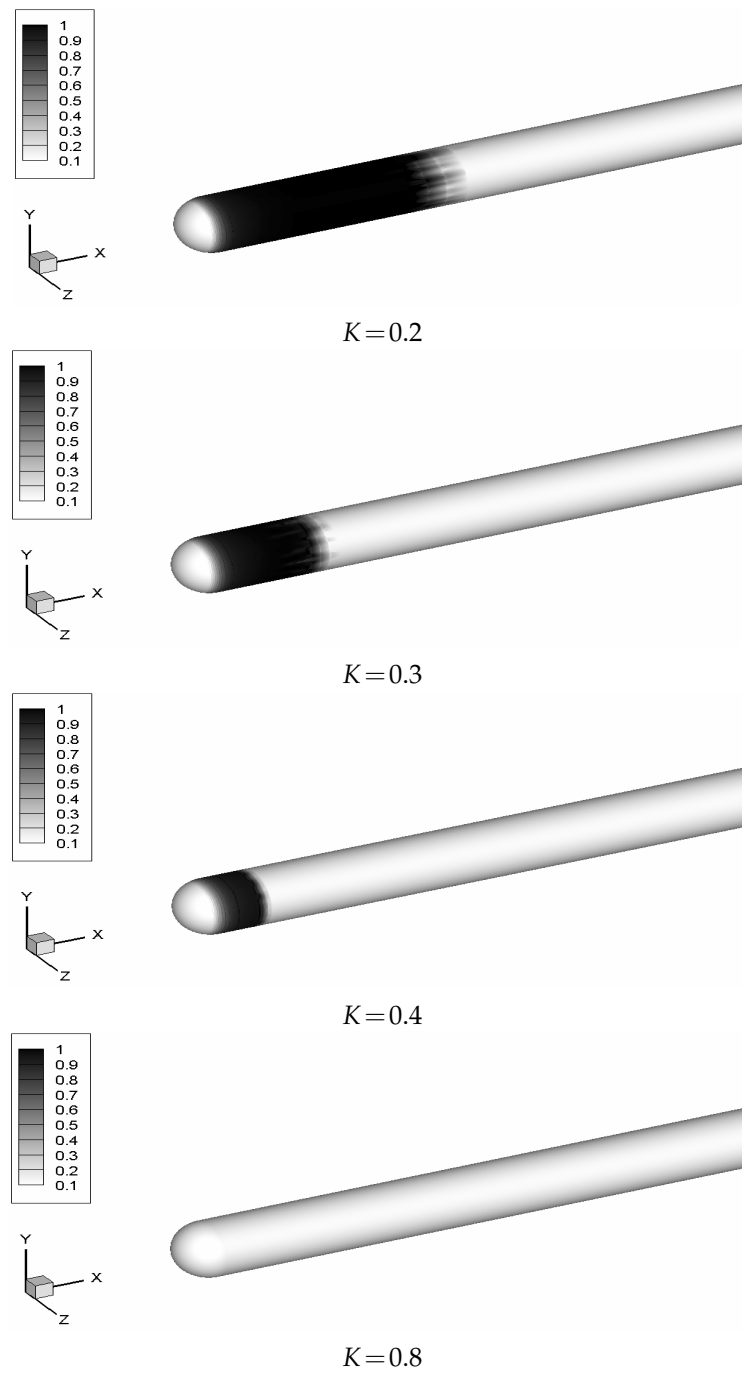


Figure 3: Three-dimensional contour plots of gas volume fraction over the cylindrical headform at steady-state ( $K=0.2\sim 0.8$ ).

Before performing the calculations, we define the cavitation number by

$$K = \frac{2(P_0 - P_v)}{(\rho U_0^2)} = \frac{P_0 - P_v}{P_0 - P_\infty},$$

where  $P_0$ ,  $P_v$ ,  $P_\infty$  are total pressure, saturated-vapor pressure, and free-stream pressure respectively. The so-called cavitation number pressure coefficient is defined as

$$C_p = \frac{2(p - p_0)}{\rho_l U_0^2}.$$

Also, the relationship between  $C_p$  and  $S/D$  are predicted in our calculations, where  $S/D$  is the surface distance starting from the head nose, normalized by its diameter of 1 in.

One of the predicted pressures in the cavitation zones is shown in Fig. 2. We can observe that the pressure of expansion region drops to the vapor pressure which leads to the formation of cavitation no matter  $K=0.2, 0.3, 0.4$ . Because of the impact of inlet liquid flow at the cylindrical head, the high local pressure regions appear around the leading edge of the head due to the local velocity near stagnation velocity. After that, the flows pass over the head shoulder, then, the local pressures continue to drop down violently, resulting in negative pressure regions which cause the appearance of the bubbles. The pressure in bubbles retained constant in the transition region of evaporation. However, for the sake of the reversal flows, the pressures rise up abruptly again at the end of the evaporation region. Here the volume fraction of the liquid is increased and the bubbles start to collapse until the bubble region disappearing. Finally, the liquid flows dominate the downstream and the pressure recovers to the initial state. When  $K=0.8$ , the pressure loss is not obvious and still larger than the local saturation pressure so that the cavitation will not be produced. As shown in Fig. 3, the evolutions of volume fraction for the water vapor are predicted in the 3D cases with  $K=0.2$  to  $0.4$  and demonstrated by the gas volume fraction fields. As  $K$  decreases from  $0.8$ , the pressure in the expansion region drops to the vapor pressure, resulting in the generation of a vapor phase and the growth of a bubble. The reversal flow appears because the negative pressure exists on the downstream. The flow velocity here is relatively small. From Fig. 3, we note that the cavitation length is getting bigger and the peak pressure is increasingly changed as the cavitation number  $K$  decreases. In addition, no cavitation zone is found in the case of  $K=0.8$ .

Fig. 4 demonstrates that the predicted surface pressure distributions, which are compared with experimental data, can also be parameterized as a function of the cavitation number. It compares the surface pressure distribution with the data of Rouse and Mc-Nown. The current test results are shown to be consistent with the validated data when  $K=0.4$  and  $K=0.8$  on both coarse grids and fine grids. However, predicted surface pressure coefficients in the phase transition regions at  $K=0.2$  and  $K=0.3$  are not completely consistent with the experimental data, although demonstrated in a satisfactory tendency. Also, an evolution of two-dimensional contour plots of gas volume fraction over the cylindrical headform at transient states for the case of  $K=0.2$  is demonstrated in Fig. 5.

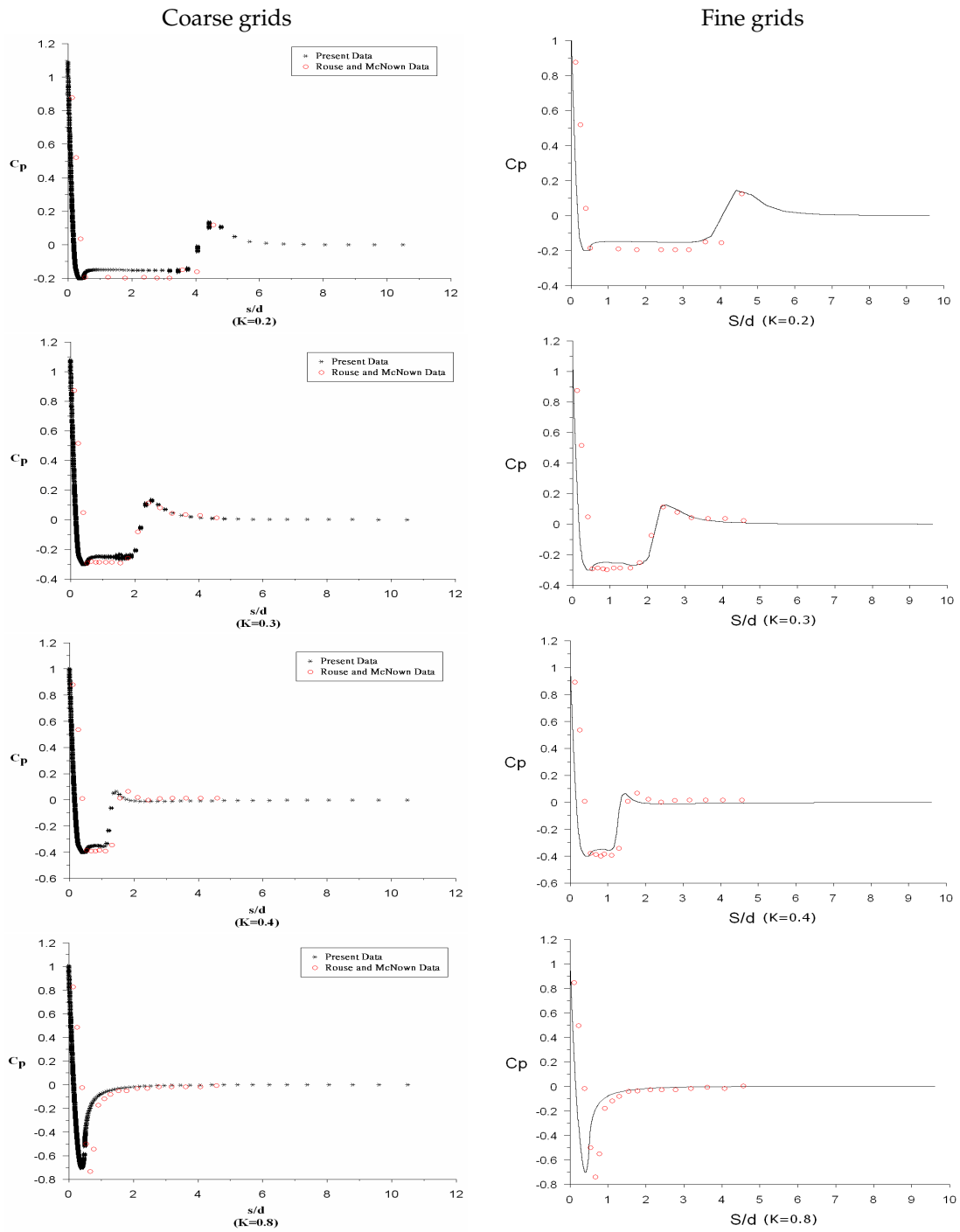


Figure 4: Surface pressure coefficient distributions ( $K = 0.2 \sim 0.8$ ) computed on  $60 \times 50 \times 100$ , coarse and  $60 \times 75 \times 200$  fine grid points.

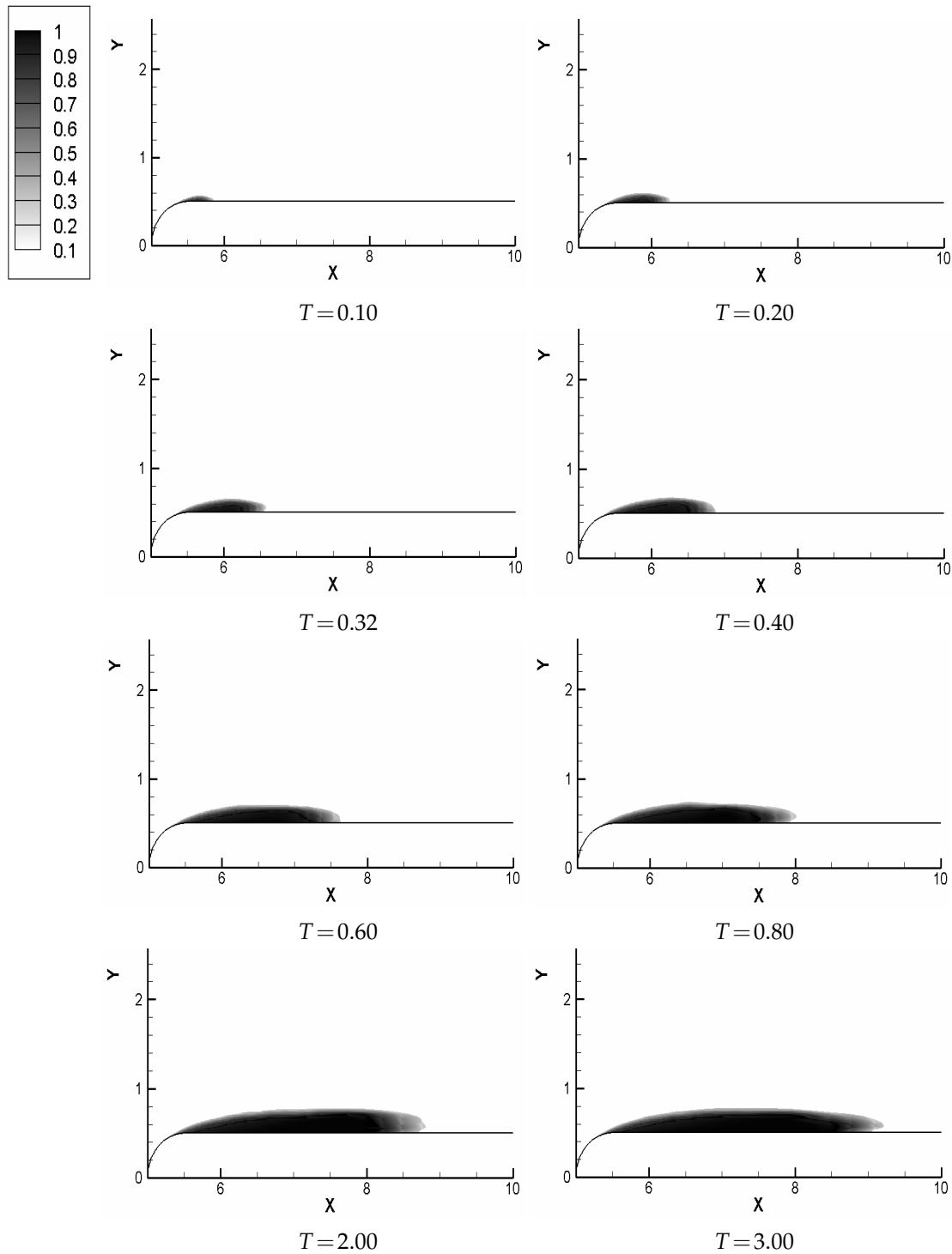


Figure 5: Three-dimensional contour plots of gas volume fraction over the cylindrical headform at transient states for the case of  $K=0.2$ .

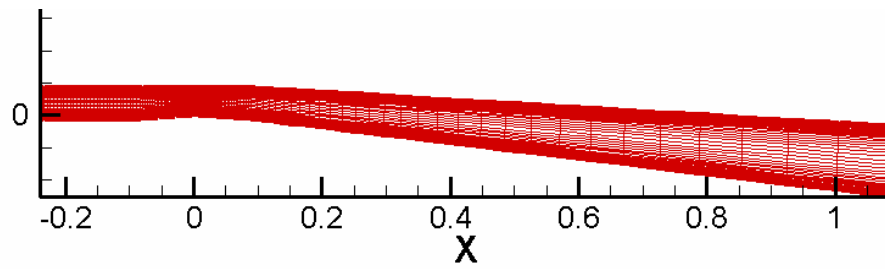


Figure 6: 2D mesh distributions of a convergent/divergent channel.

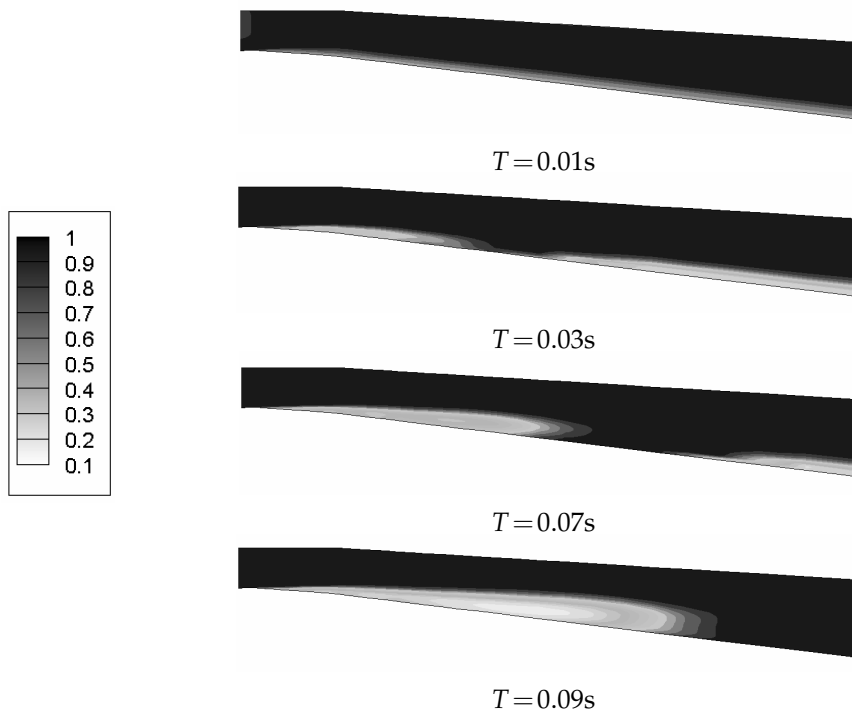


Figure 7: The contour plots of gas volume fraction for a convergent-divergent channel at different transient states (from 0 sec to 0.09 second).

From the above computations, the discrepancy from numerical prediction against measured data may arise from the unsteady turbulence phenomena in the cavitation region. This remains to be an important topic for the further cavitation flow study.

#### 4.2 Convergent/divergent channel cavity

The second case corresponds to an experiment conducted by Reboud [24], involving liquid water flow in 2D 4.3/4 degree convergent/divergent channel geometry. The geometry and mesh are shown in Fig. 6. The channel throat which is the narrowest height is

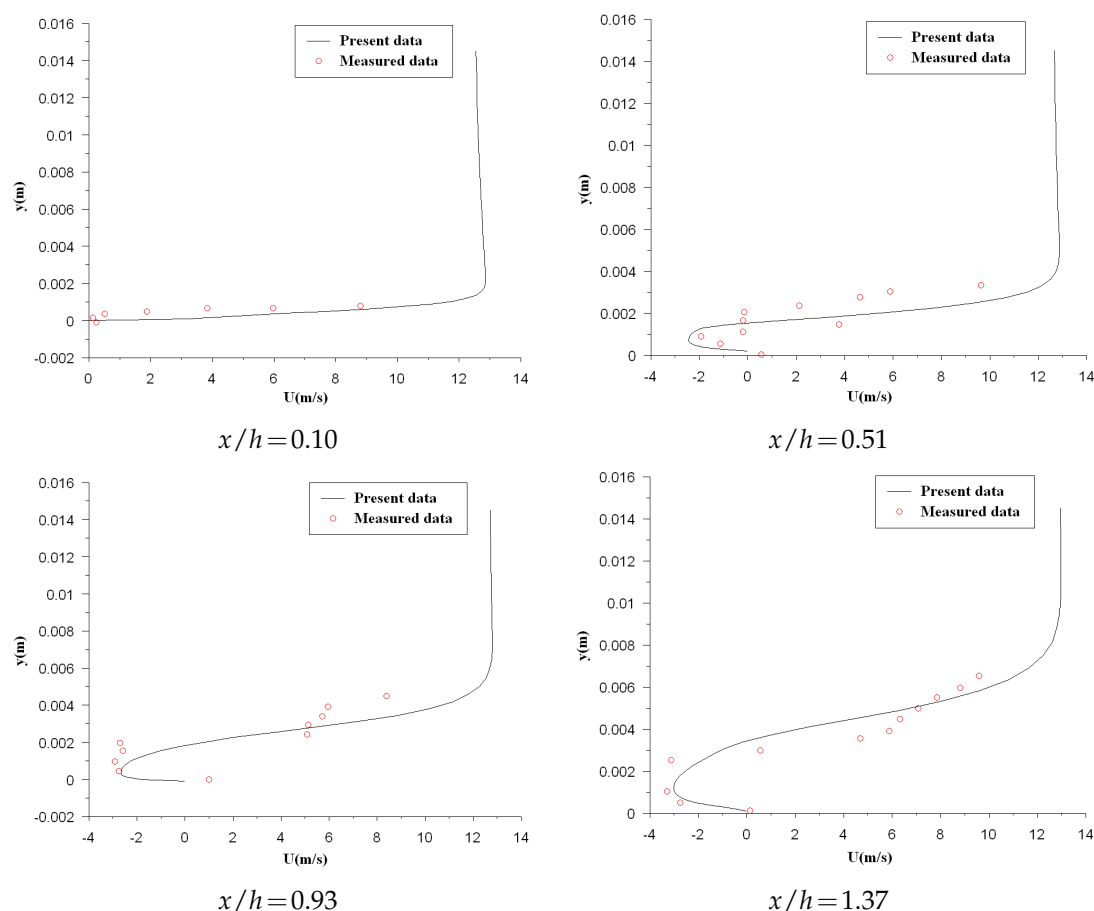


Figure 8: 2D velocity distributions of a convergent-divergent channel at different cross sections.

called  $h$ . The computations are performed on difference grids. The grid independence is found on  $160 \times 50$  grid points, with Reynolds number  $1.6 \times 10^6$ , the vapor pressure 2000 Pa, and the liquid density  $998.2 \text{ kg/m}^3$ . The computational conditions of the isothermal temperature of 293 K and inlet void fraction of 0.1% were imposed. According to Reboud's experimental observations, a nearly one periodic cycle of evaporation and condensation process was observed. In this case, the distributions of gas volume fraction are predicted as shown in Fig. 7. A thin sheet cavitation exists in vicinity of the throat and maximum volume fraction is approximately 80%. A sheet cavitation occurring near the throat developing and flowing downstream with a nearly periodic behavior is captured in our simulation. At the beginning of the gas bubble evolution, the bubble distributes like the boundary layer along the low surface in the divergent channel with the adverse pressure gradient. Then, a sheet cavity growing and getting larger from the narrow section of the throat until  $t = 0.0$  second, then repeat periodically.

Fig. 8 shows a comparison of predicted average velocity distributions against mea-

sured data. The measurement range is focused at cavitation region in which  $y$  represents the normal distance from the lower wall. Overall, the velocity profiles only agree with the measured data before the section of  $0.51h$  downstream from the throat. However, the separation region after  $0.51h$  is somewhat under-estimated. We note that the comparison is performed at very small distance scale. Therefore, our simulation actually has achieved a satisfactory tendency. Simulating velocity in the cavitated boundary layer region requires further works on the turbulence modeling.

## 5 Concluded remarks

In this work, an incompressible underwater multi-phase flow code based on the preconditioned three-dimensional multiphase Navier-Stokes equations comprised of the mixture density, mixture momentum and constituent volume fraction equations is developed. A dual-time implicit formulation with LU Decomposition is employed to accommodate the inherently unsteady physics. Also, we adopt the Roe flux splitting method to deal with flux discretization in space. Numerical validations are performed on the cases of transient 3D cylindrical headform and 2D convergent-divergent nozzle in underwater cavitating flows. Though the turbulence effects are not considered in our computations, numerical validation against experimental data in the simulation of blunt body flows is satisfactory and demonstrates a very similar surface pressure coefficient prediction as the data of Rouse and McNown [23]. A further work is required to study physical phenomena containing many sizes of length and time scales such as the turbulence effects and surface tension effects of bubbles.

## Acknowledgments

We acknowledge financial support from the National Science Council under the project NSC 96-2623-7-216-001-D. The computer facility is supported by the National Center for High-Performance Computing, Hsin-Chu, Taiwan, ROC.

## References

- [1] C. L. Merkle, J. Feng and P. E. O. Buelow, Computational Modeling of the Dynamics of Sheet Cavitation, in: Proceedings of 3rd International Symposium on Cavitation, Grenoble, France, 1998, pp. 307-311.
- [2] H. B. Stewart and B. Wendroff, Two-phase flow: Models and methods, *J. Comput. Phys.*, 56 (1984), 363-409.
- [3] W. Hirt and B. D. Nichols, Volume of fluid method for the dynamics of free boundaries, *J. Comput. Phys.*, 39 (1981), 201-225.
- [4] M. Sussman, P. Smereka and S. Osher, A level set approach for computing solutions of incompressible two-phase flows, *J. Comput. Phys.*, 114 (1994), 146-159.

- [5] D. Pan and C. H. Chang, The capturing of free surfaces in incompressible multi-fluid flows, *Int. J. Numer. Meth. Fluids*, 33 (2000), 203-222.
- [6] R. Saurel and R. Abgrall, A multiphase Godunov method for compressible multifluid and multiphase flows, *J. Comput. Phys.*, 150 (1999), 425-467.
- [7] Y.-Y. Niu, Numerical approximations of a compressible two fluid model by the advection upwind splitting method, *Int. J. Numer. Meth. Fluids*, 36 (2001), 351-371.
- [8] H. Paillère, C. Corre and J. R. García Cascales, On the extension of the AUSM+ scheme to compressible two-fluid models, *Comput. Fluids*, 32 (2003), 891-916.
- [9] C.-H. Chang and M.-S. Liou, A new approach to the simulation of compressible multifluid flows with AUSM+ scheme, *AIAA Paper 2003-4107*, 16th AIAA CFD Conference, Orlando, FL, June 23-26, 2003.
- [10] R. F. Kunz, D. A. Boger, D. R. Stinebring, T. S. Chyczewski, J. W. Lindau, H. J. Gibeling, S. Venkateswaran and T. R. Govindan, A preconditioned Navier-Stokes method for two-phase flows with application to cavitation prediction, *Comput. Fluids*, 29 (2000), 849-875.
- [11] J. R. Edwards, R. K. Franklin and M.-S. Liou, Low-diffusion flux-splitting methods for real fluid flows with phase transitions, *AIAA*, 38 (2000), 1624-1633.
- [12] I. Senocak and W. Shyy, A pressure-based method for turbulent cavitating flow computations, *AIAA*, (2001), 2001-2907.
- [13] J. W. Lindau, R. F. Kunz, D. A. Boger, D. R. Stinebring and H. J. Gibeling, High Reynolds number, unsteady multi-phase CFD modeling of sheet cavitation, *J. Fluids Eng.*, 124(3) (2002), 607-616.
- [14] V. Ahuja, A. Hosangadi and S. Arunajatesan, Numerical study of cavitation in cryogenic fluids, *J. Fluids Eng.*, 123 (2001), 331-340.
- [15] B. R. Shin, S. Yamamoto and X. Yuan, Application of preconditioning method to gas-liquid two-phase flow computations, *J. Fluids Eng.*, 126 (2004), 605-612.
- [16] A. Hosangadi and V. Ahuja, Numerical study of cavitation in cryogenic fluids, *J. Fluids Eng.*, 127 (2005), 267-281.
- [17] Y.-Y. Niu, Y.-M. Lin, Y.-C. Lin and Y.-M. Lin, A simple and robust advection upwind flux splitting to simulate transient cavitated water-vapor flows, *Numer. Heat Tran.*, 51(7) (2007), 679-696.
- [18] T. G. Liu, B. C. Khoo and W. F. Xie, The modified ghost fluid method as applied to extreme fluid-structure interaction in the presence of cavitation, *Commun. Comput. Phys.*, 1 (2006), 898-919.
- [19] B. van Leer, Upwind and high-resolution methods for compressible flow: From donor cell to residual-distribution schemes, *Commun. Comput. Phys.*, 1 (2006), 192-206.
- [20] Y. Liu, C.-W. Shu, E. Tadmor and M. Zhang, Non-oscillatory hierarchical reconstruction for central and finite volume schemes, *Commun. Comput. Phys.*, 2 (2007), 933-963.
- [21] P. L. Roe, Approximate Riemann solvers, parameter vectors and difference schemes, *J. Comput. Phys.*, 43 (1981), 357-372.
- [22] D. Pan and S. R. Chakravarthy, Unified formulation for incompressible flows, *AIAA*, (1989), 1989-0122.
- [23] H. Rouse and J. S. McNown, Cavitation and pressure distribution: Head forms at zero angle of yaw, *State Univ. of Iowa Engineering, Bulletin 32*, Ames, IA, (1948).
- [24] B. Stutz and J. L. Reboud, Two-phase flow structure of sheet cavitation, *Phys. Fluids*, 9(12) (1997), 3678-3686.